The Astrophysical Journal, 865:130 (11pp), 2018 October 1 https://doi.org/10.3847/1538-4357/aadd12

Observing the Influence of Growing Black Holes on the Pre-reionization IGM

Evgenii O. Vasiliev[1,2], Shiv K. Sethi[3], and Yuri A. Shchekinov[3,4]
[1] Southern Federal University, Rostov on Don 344090, Russia; eugstar@mail.ru
[2] Special Astrophysical Observatory, Russian Academy of Sciences, Nizhnii Arkhyz, Karachaevo-Cherkesskaya Republic 369167, Russia
[3] Raman Research Institute, Sadashivanagar, Bengaluru 560080, Karnataka, India
[4] Lebedev Physical Institute, Russian Academy of Sciences, 53 Leninsky Ave., Moscow 119991, Russia
Received 2018 June 9; revised 2018 August 22; accepted 2018 August 23; published 2018 October 1

Abstract

We consider the cosmological implications of the formation of the first stellar size black holes (BHs) in the universe. Such BHs form and grow by accretion in minihaloes of masses $\simeq 10^5$–$10^7\,M_\odot$, and emit nonthermal radiation that affects the ionization and thermal state of the intergalactic medium (IGM). We compute the implications of this process. We show that the influence regions for hydrogen increase to 10 kpc (physical length) for non-growing BHs to more than 0.3–1 Mpc for accreting BHs; the influence regions are ten times smaller for singly ionized helium. We consider three possible observables from the influence zones around accreting BHs during $8.5 < z < 25$: the H I 21 cm line, the hyperfine line of ^{3}He II, and the H I recombination lines. We show that the 21 cm emitting region around a growing BH could produce brightness temperatures $\simeq$15 mK across an evolving structure of 1 Mpc with hot, ionized gas closer to the BH and much cooler gas in outer regions. We show that current and upcoming radio interferometers such as the Low Frequency Array (LOFAR) and the Square Kilometre Array (SKA) SKA1-LOW might be able to detect these regions. The ^{3}He II emission from regions surrounding the growing BH is weak: the corresponding brightness temperatures reach tens of nano-Kelvin, which is below the range of the upcoming SKA1-MED. We show that for growing BHs, the Hα line could be detected by the *James Webb Space Telescope* with a signal-to-noise ratio of 10 in 10^4 s of integration. In light on the recent result of the Experiment to Detect the Global EoR Signature (EDGES), we show that with additional cooling of baryons owing to collision with dark matter, the H I signal could be enhanced by more than an order of magnitude.

Key words: cosmology: theory – dark ages, reionization, first stars – early universe – radio lines: general

1. Introduction

The probes of the epoch of reionization (EoR) and cosmic dawn remain outstanding aims of modern cosmology. While relevant information about the era of cosmic dawn remains elusive, important strides have been made in understanding the EoR since 2000, mainly owing to the detection of the Gunn–Peterson effect at $z \simeq 6$ and the cosmic microwave background (CMB) temperature and polarization anisotropies by the *Wilkinson Microwave Anisotropy Probe* (*WMAP)* and the *Planck* spacecraft (Fan et al. 2006; Planck Collaboration et al. 2016). The discovery of the Gunn–Peterson trough indicates that the universe might be transitioning from fully ionized to neutral at $z \simeq 6$. The CMB anisotropy measurements are consistent with the universe being fully ionized at $z \simeq 8.5$. The current best bounds on the reionization redshift from *Planck* place strong constraints on the reionization redshift, $z_{\rm reion} = 8.5 \pm 1$ (Planck Collaboration et al. 2016).

Theoretical estimates show that the first stars in the universe might have formed at $z \simeq 65$ (Naoz et al. 2006), thereby ending the dark age of the universe. The emission of UV light from these structures carved out ionized regions that might have percolated at $z \simeq 9$ (see, e.g., Barkana & Loeb 2001, and references therein). However, the nature of these first sources that ionized and heated the IGM is difficult to establish within the framework of current theoretical models. The two mostly likely candidates are star-forming halos and the precursors of quasars. In the latter case, the emission could be dominated by accretion onto a seed stellar-mass black hole (BH), which is the case we consider in this paper.

One way to probe this phase is through the detection of the redshifted hyperfine transition of neutral hydrogen (H I) from this era. The past decade has seen major progress in both theoretical and experimental efforts in this direction. Theoretical estimates show that the global H I signal is observable in both absorption and emission with its strength in the range −200–20 mK in a frequency range of 50–150 MHz, which corresponds roughly to a redshift range $25 > z > 8$ (e.g., Madau et al. 1997; Tozzi et al. 2000; Gnedin & Shaver 2004; Sethi 2005; Pritchard & Loeb 2008; Cohen et al. 2017). The fluctuating component of the signal is likely to be an order of magnitude smaller on scales in the range 3–100 Mpc (comoving), which implies angular scales in the range $\simeq$1–30 arcmin (e.g., Zaldarriaga et al. 2004; for reviews, see, e.g., Furlanetto et al. 2006; Morales & Wyithe 2010; Zaroubi 2013). Many current and upcoming experiments have the the capability to detect this signal in hundreds of hours of integration (e.g., Morales 2005; McQuinn et al. 2006; Pen et al. 2009; Parsons et al. 2012; Mesinger et al. 2014; Ahn et al. 2015; Kulkarni et al. 2016). Upper limits on the fluctuating component of the H I signal have been obtained by many ongoing experiments: the Giant Metrewave Radio Telescope (GMRT), the Murchison Widefield Array (MWA), the Precision Array for Probing the Epoch of Reionization (PAPER), and the Low Frequency Array (LOFAR; Paciga et al. 2013; Ali et al. 2015; Beardsley et al. 2016; Patil et al. 2017).

In addition to the redshifted hyperfine line of H I, it might be possible to probe cosmic dawn and EoR using other spectral lines of the primordial gas. Therefore, we also consider the H I recombination lines and the hyperfine line of ^{3}He II.

In this paper, we consider the impact of a growing BH on the thermal and ionization state of the IGM in the redshift range $8 < z < 25$. There is copious observational evidence of the

existence of supermassive BHs (SMBHs) with masses up to $M \sim 10^9\,M_\odot$ at $z \simeq 7$ (see, e.g., Mortlock et al. 2011; Venemans et al. 2013, 2015; Wu et al. 2015; Matsuoka et al. 2016; Bañados et al. 2017).[5] The presence of such "monstrous" BHs in the young universe with ages younger than 500 Myr seems challenging because of strong radiative and wind feedback (see in Khandai et al. 2015; Sijacki et al. 2015; Latif & Ferrara 2016; Rosas-Guevara et al. 2016; Volonteri et al. 2016; Gaspari & Sądowski 2017; Negri & Volonteri 2017; Latif et al. 2018; Weinberger et al. 2018). In this paper we address the question of whether the regions around these growing BHs can be observed in 21 cm emission, in the helium hyperfine line, and in hydrogen recombination lines.

In the next section, we describe our model of photon emission from a BH that forms in the redshift range 20–25 and subsequently grows owing to accretion. In Section 3 we discuss possible observables that can probe the thermal and ionization evolution of gas that is influenced by emission from the BH. In Section 4 we present our main results. In Section 5 we summarize our findings and make concluding remarks. Throughout this paper, we assume a spatially flat ΛCDM model with the following parameters: $\Omega_m = 0.254$, $\Omega_B = 0.049$, $h = 0.67$, and $n_s = 0.96$, with the overall normalization corresponding to $\sigma_8 = 0.83$ (Planck Collaboration et al. 2016).

2. Description of the Model

The accretion onto a BH is assumed to be a source of UV/X-ray photons. SMBHs with masses $\gtrsim 10^9\,M_\odot$ are known to exist at redshifts as high as $z > 7$ (Mortlock et al. 2011; Bañados et al. 2017). One can expect that during their growth phase, their predecessor contributed to heating and ionization of the universe. In order for a stellar-mass BH seed to grow to a $10^9\,M_\odot$ SMBH, a nearly continuous accretion with the Eddington rate is the most efficient regime, under which the BH mass $M_{\rm BH}$ grows as (Shapiro 2005; Volonteri & Rees 2005, 2006)

$$M_{\rm BH}(t) = M_{{\rm BH},t\,=\,0}\exp\left(\frac{1-\epsilon}{\epsilon}\frac{t}{t_E}\right), \quad (1)$$

where $M_{{\rm BH},t=0}$ is the initial BH mass and $t_E = 0.45$ Gyr, ϵ is the radiative efficiency—the efficiency of converting the rest-mass energy into luminous energy by accretion onto a BH of mass M (Shapiro 2005), $\epsilon \simeq 0.1$ is taken as a fiducial value; we discuss the impact of varying ϵ in later sections. Following Shapiro (2005), we assume that the efficiency of accretion luminosity $\epsilon_L \equiv L/L_E$, where L_E is the Eddington luminosity, is equal to unity in our calculations; $\epsilon_L = 1$ is thought to represent the upper observed limit of the quasar luminosity (McLure & Dunlop 2004).

The spectrum of the ionizing radiation emitted during accretion is assumed to be a power law,

$$L_\nu = L_0\left(\frac{\nu}{\nu_{\rm H}}\right)^\alpha, \quad (2)$$

where $\alpha = -1.5$, which is assumed to be a fiducial value in our calculations, L_0 is a normalization coefficient that is obtained for the bolometric luminosity of the BH: $L_{\rm BH} = 1.25 \times 10^{38}\,M_{\rm BH}\,{\rm erg\,s^{-1}}$ in the energy range from 13.6 to 10^4 eV. The bolometric luminosity is assumed to be equal to the Eddington limit. The spectral energy distribution slope of active galactic nuclei is measured to range from -1.7 to -1.4 (Telfer et al. 2002; Scott et al. 2004; Shull et al. 2012; Stevans et al. 2014; Lusso et al. 2015), and we consider below how this affects our results.

Current theoretical models of the first stars (Population III) in the universe favor the initial mass function (IMF) to be dominated by massive objects in the range from tens to hundreds of solar masses (e.g., Abel et al. 2002; Bromm et al. 2002; Yoshida et al. 2008). In the lower mass end (tens of solar masses), stars can form either thorugh various feedbacks (Tan & McKee 2004; Hosokawa et al. 2011) or through atomic cooling in metal-free gas with a virial temperature $T > 10^4$ K (e.g., Becerra et al. 2015), or owing to cooling by metals/dust in a weakly enriched gas (e.g., Bromm et al. 2001; Dopcke et al. 2013).

The seeds for BHs are the final product of the evolution of Population III stars with $M \sim 30$–$260\,M_\odot$ (see, e.g., Woosley et al. 2002). Low-mass stars, $M \sim 30\,M_\odot$, are likely more numerous and might be more common seeds for BHs. However, only a small mass fraction ∼10% of their progenitors collapses to form a BH, and therefore these stars do not contribute significantly to the growth of SMBHs. Even though this fraction increases for higher mass stars, it still remains smaller than 50% for $M \lesssim 100\,M_\odot$. However, stars with $M \gtrsim 260\,M_\odot$ leave remnants—BHs that are only slightly less massive than the progenitor. The Eddington rate is relatively slow: as seen from Equation (1), accretion with $\epsilon = 0.1$ increases the BH mass by factor 10 from $z = 50$ to $z \simeq 20$ and by 30 to $z \simeq 17$. Therefore, only stellar progenitors of $M \gtrsim 260\,M_\odot$ are capable of giving rise to SMBHs. Based on these considerations, in our calculations, we adopt $M_{\rm BH} = 300\,M_\odot$ as the fiducial value for BH seeds, although deviations from this value are also discussed. It is worth noting that in low-mass halos (apparently $<10^6\,M_\odot$ Park Ricotti 2011; Jeon et al. 2012; Whalen & Fryer 2012), radiative and mechanical feedback can inhibit an SMBH from growing from a stellar-mass BH seed. However, currently there are too few numrical simulations to firmly conclude about inhibitive feedbacks on the growth of SMBHs into more massive $\geqslant 10^8\,M_\odot$) minihalos (Wise 2018).

Stellar progenitors of BHs are formed in minihalos with total masses $M \sim 10^5$–$10^7\,M_\odot$ (Haiman et al. 1996; Tegmark et al. 1997; see also the review Barkana & Loeb 2001). Eventually, depending on specific conditions in a minihalo, a single very massive star or/and several less massive stars do form and produce a copious amount of ionizing photons (Tumlinson & Shull 2000; Bromm & Larson 2004). As a result, a significant fraction of gas in the host minihalo becomes ionized, and the escape fraction of Lyman continuum photons into the IGM can grow substantially (see the review by Ciardi & Ferrara 2004; Ferrara & Loeb 2013).

To model absorption of ionizing photons inside the halo, we assume that average total column density of H I inherent to the host galaxy is $N^h_{\rm H\,I}$, with a primordial abundance of elements: $X = 0.76$ and $Y_{\rm He} = 0.24$. In our calculations we include absorption not only in the host galaxy, but in the circumgalactic gas within several virial radii (≃1–3) as well. The neutral hydrogen fraction in the ISM of the host halo is determined by a detailed evolution of the halo, e.g., gas coolng/heating,

[5] http://www.homepages.ucl.ac.uk/~ucapeib/list_of_all_quasars.htm

possible star formation, and BH feedbacks. On the other hand, the density and velocity profiles outside the halo might be altered by tidal interactions and merging with other halos. Therefore, finding a closer connection between $N^h_{\rm H\,I}$ and the underlying galactic ISM is very challenging (see, e.g., Bromm et al. 2003; Whalen et al. 2004; Greif et al. 2007; Vasiliev et al. 2008; Whalen et al. 2008; Vasiliev et al. 2012), and this is beyond the scope of the paper. However, it is obvious that on much larger scales where the diagnostics discussed in this paper arise, e.g., the 21 cm signal, the details of the gas distribution around the host halo play a minor role and only the average value of $N^h_{\rm H\,I}$ might suffice to model the absorption inside the halo.

Therefore, we consider several values for $N^h_{\rm H\,I}$ to model the host halo, with $N^h_{\rm H} = 10^{20}\,{\rm cm}^{-2}$ as a fiducial value. This choice is consistent with the fact that the total column density of minihalos with $M \lesssim 10^9\,M_\odot$ formed at $z \simeq 10$–20 is lower than $10^{21}\,{\rm cm}^{-2}$ (assuming the top-hat density profile, for simplicity). As we expect the gas inside halos to be partially ionized by both stellar progenitors and the BH itself, the adopted value of the H I column density seems a reasonably conservative estimate. In Section 4.2 we discuss the dependence of our results on its variation.

The radiation from the growing BH can also be attenuated by neutral IGM gas. The optical depth at a distance r from the BH is $\tau_\nu(r) = \int \sigma^k_\nu(r) n^k(r) dr$, where k = H I, He I, He II, and σ^k_ν are the cross-sections at frequency ν (Cen 1992; Glover & Jappsen 2007), and the values $\sigma^k_\nu(r)$ and $n^k(r)$ depend on ionization and the thermal history of the IGM, whose evolution is described below.

Then, the flux of the ionizing radiation at a distance r from the BH is

$$F_\nu = \frac{L_\nu}{4\pi r^2}\exp(-\tau_{\rm h} - \tau_{\rm IGM}), \qquad (3)$$

where the first term in the exponent is due to the attenuation in the host galaxy (it depends on $N^h_{\rm H\,I}$ and we assume it to remain constant during the evolution), and the second term is determined by absorption in the medium surrounding the BH and the IGM.

In the hierarchical structure formation scenario, minihalos undergo mergers, in some of which the seeds of BHs with intermediate mass form, and can efficiently grow only when a considerable reservoir of gas is available. This suggests that minihalos with growing BHs undergo frequent mergers and collect a sufficient gas mass to feed the BHs. The lower the radiative efficiency during a BH growth, the higher the mass that is required to maintain growth, and this mass may sometimes exceed the initial baryon mass of the host minihalo. For instance, for $\epsilon = 0.2$, a BH mass grows about 33 times in ~400 Myr. For a seed with $M_{\rm BH} = 300\,M_\odot$, this growth can be maintained in a host minihalo as small as $M \lesssim 10^5\,M_\odot$. However, for $\epsilon = 0.1$ in the same period, the BH mass increases by about 2.5×10^3 times, whereas for $\epsilon = 0.05$, the ratio reaches values as high as 1.5×10^7. Therefore, only minihalos with an accretion rate higher than $\dot{M} \geqslant 0.4\,M_\odot\,{\rm yr}^{-1}$ could host growing BH with such a low radiative efficiency.

In the ΛCDM model, star-forming minihalos for a wide range of masses $<10^8\,M_\odot$ merge and virialize at $z \gtrsim 25$ as (3–4)σ density peaks. The merging rate of such minihalos seems to be sufficient to provide the sites for a feeding growth of massive BHs (Volonteri & Rees 2005). Based on these considerations, we start the evolution at $z_0 = 25$ and continue it for 400 Myr, which corresponds to a final redshift $z \simeq 10$, which is close to the era at which reionization of the universe is completed. Therefore we explicitly assume that BHs grow nearly with a steady-state Eddington accretion rate on cosmological timescales. In this regard, this consideration excludes the possibility of incorporating the recently widely discussed direct monolithic collapse of SMBHs (Begelman et al. 2006), as they apparently keep the accretion rate close to the Eddington limit only on a very short timescale, ~1 Myr after formation (see, e.g., Johnson et al. 2011).

How numerous might high-redshift BHs be? The space density of halos that can host BHs at high redshifts can be computed using the Press–Schechter formalism. Assuming a typical halo mass of $10^7\,M_\odot$, the comoving density of such haloes increases from $10^{-2}\,{\rm Mpc}^{-3}$ to nearly $1\,{\rm Mpc}^{-3}$ in the redshift range 10–20 (e.g., Barkana & Loeb 2001). However, the conversion of the space density of haloes that can host BHs into the number density of BH precursors is highly uncertain. Their comoving density could lie in the range 10^{-3}–$10^{-10}\,{\rm Mpc}^{-3}$ at $z \simeq 10$ (e.g., Figure 4 of Dijkstra et al. 2014).

Two AGNs have been detected at $z > 7$, and they host BHs with $M \simeq 10^9\,M_\odot$. If these BHs grew from stellar seeds, the growth could have commenced at $z \simeq 14$ to reach $M \simeq 10^9\,M_\odot$ within one Eddington time (0.45 Gyr, which is close our final time in calculations) for $\epsilon = 0.05$. At lower redshifts ($z \simeq 2$–4), such AGNs have absolute magnitudes in the range −26 to −28 (see Figure 5 in McLure & Dunlop 2004 and Figure 13 of Palanque-Delabrouille et al. 2013). Less massive BHs $M \simeq 10^8\,M_\odot$ are expected to be more than one hundred times more numerous (Figure 6 in Volonteri & Rees 2006). These BHs could have emerged from the same mass halos but for higher values of ϵ.

In our mode, a minihalo with a seed BH is immersed into the IGM. The dynamical state and structure of the transition layer between the minihalo and the surrounding gas can in general be complicated, with an inhomogeneous distribution of the gas density, temperature, and velocity field. We neglect the complications of this narrow interface and match the minihalo directly to the IGM, starting our calculations from the internal boundary of the surrounding intergalactic gas. We assume this gas to have a homogeneously distributed density and a temperature that decreases as a result of cosmological expansion: $\propto(1+z)^{-3}$ and $\propto(1+z)^{-2}$, until the ionizing radiation from a BH changes its thermodynamics.

We consider the evolution of gas enclosed in the concentric static spheres with a BH in the center. The radii of spheres extend from 10^3 to 10^7 pc (all distances are expressed in physical units unless otherwise specified). The radii of neighboring spheres differ by a factor $a_r = 1.1$: $r_{i+1} = a_r r_i$, which yields 100 concentric shells that account for the ratio of outer radius to inner radius. Note that the inner radius is about three times greater than the virial radius of a minihalo with $M = 10^7\,M_\odot$ formed at $z = 20$ (e.g., Ciardi & Ferrara 2004).

In each sphere we solve the thermal and ionization evolution of hydrogen, neutral helium, and singly ionized helium. We consider the following processes for primordial plasma: collisional ionization, recombination, and photoionization by UV/X-ray radiation from the BH attenuated by both the host galaxy and the surrounding IGM gas. The thermal evolution includes cooling due to collisional ionization for H I, He I, and

He II, recombination of H II, He II (radiative and dielectronic), and He III, collisional excitation of H I, He I (1^2S and 2^3S), and He II, free–free emission and Compton cooling/heating, and photoionization heating. The reaction and cooling/heating rates are taken from Cen (1992) and Glover & Jappsen (2007). Because we consider ionization by X-ray radiation, the influence by secondary electrons is taken into account as described in Shull & van Steenberg (1985) and Ricotti et al. (2002). In the equation of the thermal evolution, we add the cooling term that is due to the Hubble expansion, in order to correctly describe the evolution on timescales that are greater than the local age of the universe. We solve the equations on a timescale 400 Myr, such that for the initial redshift $z_0 = 20$, our calculations are complete at 8.5. The initial gas temperature and H II fraction for a given redshift are obtained using the RECFAST code (Seager et al. 2000), while helium in the initial state is assumed to be neutral.

3. Observable Features of Cosmic Dawn and EoR

In this section we discuss in detail the possible observables in the redshift range $8.5 < z < 25$ owing to the impact of radiation from the accreting BH.

3.1. 21 cm Line

Atomic collisions and scattering of UV photons couple the H I spin temperature to the gas kinetic temperature, T_k, and to the color temperature, T_c (Wouthuysen 1952; Field 1958):

$$T_s^{\rm H\,I} = \frac{T_{\rm CMB} + y_c T_k + y_a T_c}{1 + y_c + y_a}. \quad (4)$$

Here y_c and y_a determine the coupling of the two states of the H I hyperfine splitting owing to collisions and Lyα photons (Wouthuysen–Field coupling), respectively; $y_c = C_{10}^{\rm H\,I} T_\star / (A_{\rm H\,I} T)$ with $T_\star = h\nu_{\rm H\,I}/k$ and $C_{10}^{\rm H\,I}$ being the collisional de-excitation rate of the hyperfine line of H I. We assume that the color temperature is coupled to the gas kinetic temperature: $T_c \simeq T_k$.

The coefficient y_a is similarly defined with collisional de-excitation rate replaced with the de-excitation rate owing to Lyα photons. Given the geometry of our physical setting, the coupling of the expanding gas with Lyα photons from the BH needs to be discussed in detail. Lyα photons in the rest frame of a BH are strongly absorbed in the halo of column density $N_{\rm H\,I} \simeq 10^{20}\,{\rm cm}^{-2}$ surrounding the BH as the line center cross-section for Lyα scattering is $\simeq 10^{-13}\,{\rm cm}^2$ (assuming a temperature $T \simeq 5000$ K). Using a Voigt profile, one can show that photons of frequencies $\nu \simeq \nu_\alpha \pm 50\Delta\nu_D$, where $\Delta\nu_D = \nu_\alpha / c(2kT/m_p)^{1/2} \simeq 10^{-5}\nu_\alpha$ is the Doppler width, can escape the halo. As the medium outside the halo is expanding, the photons will redshift, and photons with frequencies higher than Lyα in the BH rest frame can be absorbed in the expanding medium. Using the local Hubble law, $v = H(z)r$, one can show that these photons are absorbed in a range of distances 0.01–1 Mpc from the halo.

This motivates us to assume that the number of Lyα photons (which are photons with frequencies marginally above Lyα in the BH rest frame) in the expanding medium suffer only geometric $1/r^2$ dilution. In addition, we also assume that in situ injected Lyα photons emerge due to recombinations with a number density that is proportional to the local photoionization rate (see Equations (15) and (17) in Chen & Miralda-Escudé 2004). Following Field (1958), we here also explicitly assume the "color temperature" of Lyα photons to be equal to the gas kinetic temperature.

In the collisional de-excitation rate we take into account collisions with H atoms (Kuhlen et al. 2006) and electrons (Liszt 2001). y_a is proportional to the number density of Lyα photons at the point of scattering.

The differential brightness temperature for the redshifted H I line can be estimated (Chen & Miralda-Escudé 2004; Furlanetto et al. 2006) as

$$\Delta T_{\rm H\,I}^b = 25\ {\rm mK}(1+\delta)\frac{n_{\rm H\,I}}{n}\ \frac{T_s^{\rm H\,I} - T_{\rm CMB}}{T_s^{\rm H\,I}}\left(\frac{\Omega_b h}{0.03}\right) \times \left(\frac{0.3}{\Omega_m}\right)^{0.5}\left(\frac{1+z}{10}\right)^{0.5}\left[\frac{H(z)/(1+z)}{dv_\parallel/dr_\parallel}\right], \quad (5)$$

where δ is the overdensity, which is neglected as we assume uniform Hubble expansion at high redshifts so that the gradient of the proper velocity along the line of sight $dv_\parallel/dr_\parallel$ equals $H(z)/(1+z)$. Near the halos hosted by BHs, the line broadening is dominated by peculiar velocities of the IGM gas rather than the Hubble expansion. In this case, the center-of-line optical depth and consequently the brightness temperature $\Delta T_{\rm H\,I}^b$ decrease.

3.1.1. Global Condition of H I Absorption from EDGES Observations

In this work, we model the H I signal from gas surrounding an isolated accreting BH. Such BHs are not the only source that can emit UV radiation relevant for modeling H I absorption and the emission signal from high redshift. While we do not incorporate in our models all other possible sources in the redshift range of interest, it is important to know the physical state of gas far from the zone of influence of the BH. This would allow us to smoothly match the H I signal from regions close to the BHs to the signal expected from ambient gas under global conditions.

Recent EDGES observations (Bowman et al. 2018) show a sky-averaged absorption feature of strength $\Delta T \simeq -500$ mK in the frequency range 70–90 MHz, which corresponds to a redshift range 15–19 for the redshifted H I line.

The minimum temperature of the IGM at $z \simeq 19$ is $T \simeq 6$ K in the usual case (standard recombination history), and it follows from Equation (5) that the absorption trough in the redshifted H I hyperfine line at $z \simeq 19$ should not have been deeper than about -180 mK. One plausible explanation of the EDGES results relates to overcooling of baryons by elastic collisions with dark matter particles, as suggested by Barkana (2018). In this case, as seen in Equations (4) and (5): (*a*) Lyα photons globally couple the spin temperature to matter temperature, i.e., $Ty_\alpha \gg T_{\rm CMB}$, such that $T_s = T$ at $z \simeq 19$, and (*b*) $T_s \ll T_{\rm CMB}$ as the signal is seen in absorption and is strong. Note that this explanation is still widely debated, however, because of a possible systematic error of the EDGES result (Hills et al. 2018). Another possible alternative explanation might be that there is additional radio background at $z \simeq 18$ whose temperature $T_{\rm radio}$ is higher than the CMB temperature; in this case, we can replace $T_{\rm CMB}$ with the $T_{\rm CMB}+T_{\rm radio}$ in Equation (5) (Feng & Holder 2018) and the enhancement of the observed signal is not due to the cooling of baryons. It is also conceivable that the observed feature is caused by radiation from spinning dust grains in the Galactic ISM (Draine & Miralda-Escudé 2018). We explore here the

implications of coupling between DM and baryons as a possible explanation of the EDGES result.

To model the global conditions implied by the EDGES observations, we solve one more equation for the dark matter temperature, $T_{\rm dm}$, which can be altered through adiabatic expansion and the interaction with baryons. In addition, the term corresponding to the interaction of matter with dark matter is added to the matter temperature equation as well (for details, see, e.g., Barkana et al. 2018). We follow Barkana et al. (2018) in modeling $\sigma_{\rm dm}$, the energy-exchange cross-section between dark matter and matter, as following the form of Rutherford scattering between a millicharge dark matter particle with electrons (e.g., Chuzhoy & Kolb 2009; McDermott et al. 2011; Dvorkin et al. 2014; Berlin et al. 2018; Muñoz & Loeb 2018). In this case, $\sigma_{\rm dm} = 8\pi g^2 e^4/(m_e m_{\rm dm} v^4)\log(\Lambda)$, where g is the ratio of dark matter charge to electron charge. v is the relative velocity between the two particles, and $\langle\sigma_{\rm dm} v\rangle$ corresponds to thermal averaging. The most significant aspect of such an interaction for our purposes is that it is proportional to $1/v^4$. At higher redshifts when the temperature is higher, the interaction is therefore negligible. $n_{\rm dm}$, the number density of dark matter particles, is another free parameter, $n_{\rm dm} = \rho_{\rm dm}/m_{\rm dm}$.

As there are three free parameters in modeling this interaction—the number density of the dark matter particle (or equivalently, the mass of the dark matter particle), the interaction strength between dark matter and baryons, and the initial temperature of dark matter—a rich array of possible scenarios is possible (for details, see, e.g., Barkana et al. 2018). It is not our aim here to constrain these parameters, but obtain the global condition of the H I gas in the redshift range of interest. To cool the baryons at $z \simeq 20$, we require $n_{\rm dm}\sigma_{\rm dm} v > H$, where H is the expansion rate of the universe. Using the expression for $\sigma_{\rm dm}$ given above, v as the average speed of thermal electrons at $z \simeq 20$ before the additional cooling sets in, and assuming 1% of the DM to be millicharged, we obtain $g > 10^{-7}$ for $m_{\rm dm} \simeq 10$ MeV, in agreement with the results of Barkana et al. (2018).

We also need a global heating source that allows H I to heat above the CMB temperature for $z < 15$, as the EDGES observations require. We add a corresponding term that gives an additional heating source for global heating; this term is modeled as photoelectric heating by X-ray photons from sources except for the BH (see, e.g., Fialkov et al. 2014, 2018; Cohen et al. 2017).

As noted above, an essential component of our modeling of the EDGES result is $T_s^{\rm H\,I} = T$ in Equation (4). All the parameters (global heating rate, cross-section of dark matter-baryon scattering, and Lyα coupling) have been chosen to fit the 21 cm brightness temperature $T_b \sim -500$ mK at $z \sim 20$ as in Bowman et al. (2018).

3.2. ^{3}He II Hyperfine Line

Another important hyperfine structure transition exists in the singly ionized helium-3 isotope ^{3}He II at 8.67 GHz (Townes 1957; Sunyaev 1966; Goldwire & Goss 1967; Rood et al. 1979; Bell 2000; Bagla & Loeb 2009; McQuinn & Switzer 2009; Takeuchi et al. 2014). Similar to the H I hyperfine line, this transition is excited by collisions with atoms and electrons and by photon scattering. The rate of transition owing to collisions for singly ionized helium-3 with electrons is given by

$$C_{10}^{^3\rm He\,II} = n_e\left(\frac{kT}{\pi m_e c^2}\right)^{1/2} c\sigma_e^{^3\rm He\,II}, \tag{6}$$

where $\sigma_e^{^3\rm He\,II}$ is the average cross-section of the spin exchange between ^{3}He II and electrons, which is approximated as (McQuinn & Switzer 2009)

$$\sigma_e^{^3\rm He\,II} \simeq \frac{14.3\rm eV}{kT} a_0^2, \tag{7}$$

where a_0 is the Bohr radius. In this case, the Wouthuysen–Field coupling between the two levels is caused by photons of wavelength $\lambda = 304$ Å (Equation (17) in McQuinn & Switzer 2009). The number density of these photons at the point of scattering is computed from the spectrum of BH emission. This allows us to calculate the differential brightness temperature of the ^{3}He II line using Equation (4):

$$\Delta T_{^3\rm He\,II}^b = 1.7 \times 10^{-3}\ \rm mK\ (1+\delta)\ \frac{n_{He\,II}}{n} \times \frac{T_s^{^3\rm He\,II} - T_{\rm CMB}}{T_s^{^3\rm He\,II}} \left(\frac{Y_{^3\rm He}}{10^{-5}}\right)\left(\frac{\Omega_b h}{0.03}\right) \times \left(\frac{0.3}{\Omega_m}\right)^{0.5}\left(\frac{1+z}{10}\right)^{0.5}\left[\frac{H(z)/(1+z)}{dv_\parallel/dr_\parallel}\right], \tag{8}$$

where $Y_{^3\rm He}$ is the primordial abundance of the helium-3 isotope, which is assumed to be equal 10^{-5}, and $n_{\rm He\,II}$ is the number density of the singly ionized helium-4 isotope.

3.3. Optical and Radio-recombination Lines

As seen in Figure 1, growing BHs produce regions of high ionization that may be detected in hydrogen recombination lines.

The frequencies of Hnj lines are $\nu_{{\rm H}nj} = cR\left[\frac{1}{n^2} - \frac{1}{j^2}\right]$, with $j > n$ and $R = 1.0968 \times 10^5\ \rm cm^{-1}$ being the Rydberg constant for hydrogen. The emissivity of a recombination line averaged over a sphere of radius r_i around the BH is $\epsilon_{{\rm H}nj}(r_i) = q_{nj}\alpha_j n_e(r_i) n_{\rm H\,II}(r_i)$; $n_e(r_i)$ and $n_{\rm H\,II}(r_i)$ are the number densities of e and H II species, respectively, α_j is the recombination coefficient to the jth state (for a detailed discussion and derivation, see, e.g., Rybicki & Lightman 2004), and $q_{nj} \simeq A_{jn}/\sum_{m<j} A_{jm}$ is the probability that an atom recombined to jth state emits a photon by spontaneous decay to nth state. In practice, H$n\alpha$ lines from transitions between the states n and $n+1$ are usually considered because they are the strongest with the largest A-coefficients (e.g., Rybicki & Lightman 2004).

The emissivity in these lines can be approximated as $\epsilon(r_i) \simeq 3.25 n^{-2.72}\alpha_B(r_i) n_e(r_i) n_{\rm H\,II}(r_i)$ (Rule et al. 2013), where α_B is the case B recombination rate (Equation (14.8) in Draine 2011). The total luminosity in j-line is $L_j = (hc/\lambda_j)\sum_i \epsilon_j(r_i) V(r_i)$, where V_i is the volume of i-sphere. We include all spheres with $T > 100$ K and achieve reasonable convergence for the predicted luminosity as the ionized fraction falls faster than r_i^{-2}. The flux in j-line is

$$F_{\nu_j} = \frac{1}{\Delta\nu_j}\ \frac{(1+z)L_j}{4\pi d_L^2}, \tag{9}$$

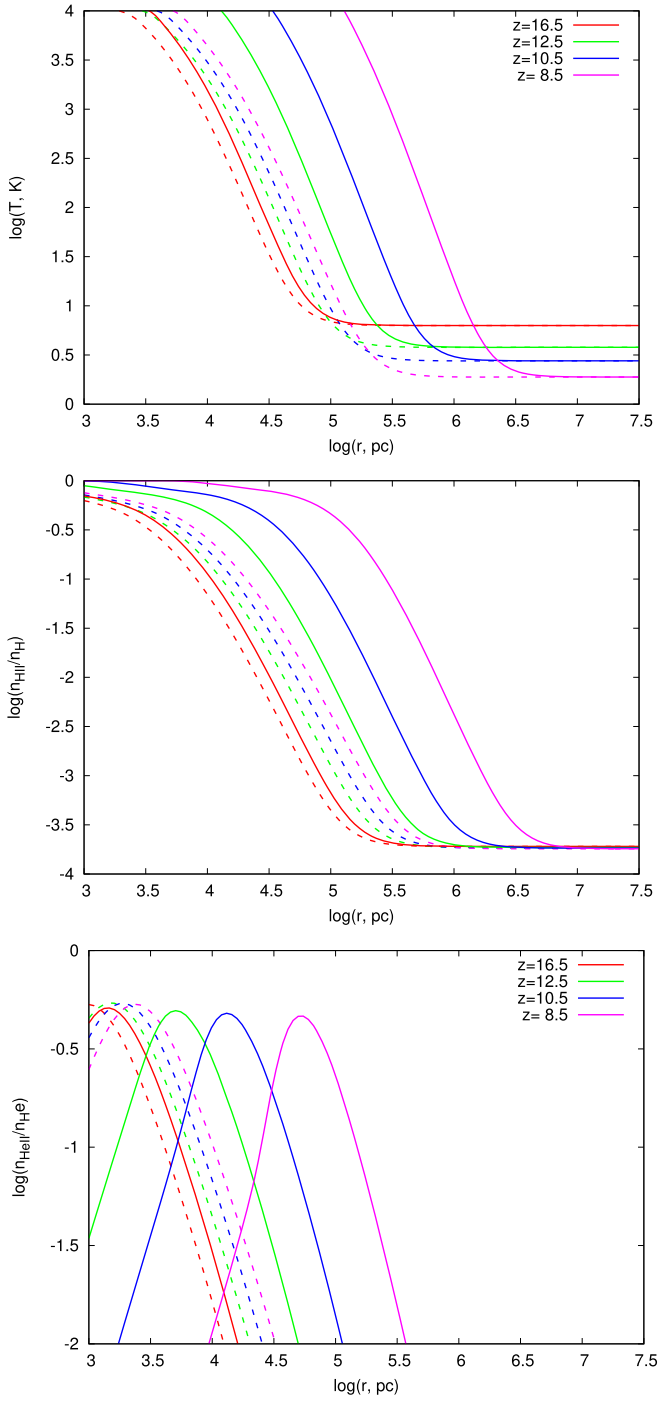

Figure 1. Radial distribution (radius is in physical, not comoving units) of the kinetic temperature (upper), H II fraction (middle), and He II fraction (lower) around a BH with initial mass $M_{\rm BH,z0} = 300\,M_\odot$ and radiative efficiency $\epsilon = 0.1$ starting its evolution at $z_0 = 20$ for several redshifts: $z = 16.5$, 12.5, 10.5, and 8.5 (lines from left to right); dashed lines represent a BH with a constant mass $M_{\rm BH} = 300\,M_\odot$.

where d_L is the luminosity distance. The line width is $\Delta\nu_j = \max(1/\sum_{i<j} A_{ni}, \Delta\nu_D)$. In all cases of interest here, Doppler broadening dominates, such that $\Delta\nu_j$ is given by Doppler line width:

$$\Delta\nu_j = \frac{\nu_{j0}}{c}\sqrt{\frac{2kT}{m_p}}. \quad (10)$$

4. Results

4.1. H I 21 cm Observables

Figure 1 shows the thermal and ionization evolution around both non-growing (constant mass) and growing BHs with an initial redshift $z_0 = 20$. The non-growing BH is surrounded by the zone of influence—the region of (physical) size $r \lesssim 10^5$ pc, in which the gas temperature and the ionized fraction of hydrogen and helium differ significantly from the background values. In the central part of $r \sim 10$ kpc, the ionized fraction of hydrogen reaches close to unity and the temperature exceeds 10^4 K. The zone of ionized gas shows a slow evolution with redshift, $r \propto t$.

The growing BH produces more ionizing photons and the zone of influence increases much faster than in the previous case, nearly as $r \propto t^{1.6}$. For $\epsilon = 0.1$, the size of a sphere where the gas temperature and ionizing fraction differ markedly from the background values, becomes larger at redshift $z = 8.5$ by more than an order of magnitude than that for a non-growing BH. The physical size of the zone of influence in the latter case grows from nearly 10 to 300 kpc during the growth of the central BH. The ionization fraction of hydrogen can reach a few percent within the region, with the temperature exceeding 300 K. The zone of influence of helium is generally smaller and reaches 100 kpc at the upper end.

First, we consider the case when the implications of EDGES results are not taken into account. Figure 2 shows radial profiles of the brightness temperature for static (dashed lines) and growing (solid lines) BHs for two different values of the radiative efficiency $\epsilon = 0.1$ and 0.05. The brightness temperature peaks in the region with a sufficiently high kinetic gas temperature T and a high fraction of atomic hydrogen, i.e., where the product $Tx_{\rm H\,I}$ peaks. Conversely, the signal from the 21 cm lline emission vanishes when Lyα coupling becomes inefficient. As seen from Equation (1), lower ϵ causes a higher accretion rate and higher luminosity. Consequently, the zones of influence are greater and the 21 cm line emission brightens at a given time, such that its appearance becomes more clearly pronounced.

Figure 3 shows the radius at which the brightness temperature in the 21 cm H I line ΔT_b reaches maximum (red lines) and the radius beyond which ΔT_b becomes negative (green lines) versus the radiation efficiency ϵ, at two redshifts: $z = 10.5$ (dashed lines) and 8.5 (solid lines) for a BH starting its evolution at $z_0 = 20$. The region that is influenced by growing BHs is clearly larger for smaller ϵ: for $\epsilon \simeq 0.05$, it extends up to $\sim$1 Mpc, corresponding to a comoving scale $\simeq$10 Mpc, which is close to the spatial resolution of current radio interferometers such as LOFAR. For $\epsilon \sim 0.1$–0.25, it reaches around 0.1 Mpc at $z \lesssim 10.5$. This is also comparable to the mean distance between minihalos with $M \gtrsim 10^6\,M_\odot$ at $z \sim 10$, which means that a growing BH can affect star formation in neighboring minihalos (Haiman et al. 2000), which can result in a stronger signal in the 21 cm line.

The evolution of this region can be represented in observable values. Figure 4 shows how the angular diameter of the region emitting in the 21 cm line depends on the observed frequency $\nu_o = 1420\,{\rm MHz}/(1+z)$ for a growing BH with a radiative efficiency $\epsilon = 0.1$ starting its evolution at redshifts $z_0 = 50$, 30, and 20. The diameter of the emitting sphere is defined as that where the brightness temperature in the 21 cm H I line

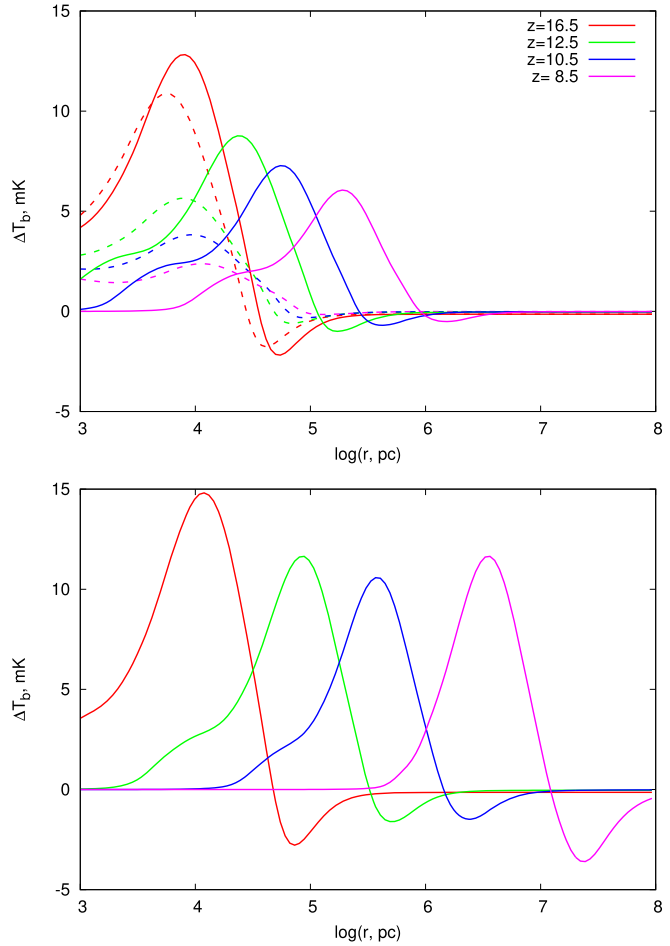

Figure 2. Brightness temperature in the 21 cm H I line as a function of radius for different cases around a BH with initial mass $M_{\rm BH,z0} = 300\,M_\odot$, starting its evolution at $z_0 = 20$ with a radiative efficiency $\epsilon = 0.1$ (upper panel) and 0.05 (lower panel). The dashed lines shown in the upper panel correspond to a non-growing BH with constant BH mass $M_{\rm BH} = 300\,M_\odot$.

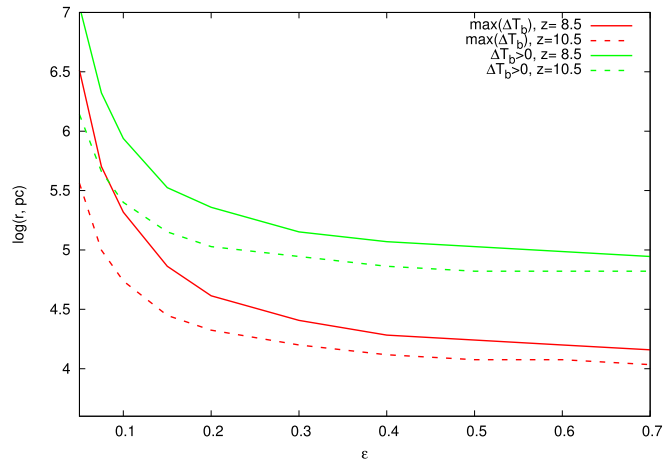

Figure 3. Radii of spheres around a BH with an initial mass $M_{BH,z0} = 300\,M_\odot$ starting its evolution at $z_0 = 20$ vs. radiative efficiency ϵ at two redshifts: $z = 10.5$ (dashed lines) and 8.5 (solid lines). The red lines show the radius at which the brightness temperature in the 21 cm H I line ΔT_b reaches maximum, and the green lines depict the radius at which ΔT_b is positive (see Figure 2).

$\Delta T_b^{\rm H\,I}$ reaches maximum (see Figure 1). One can note that the angular size of the regions becomes greater than 1 arcmin at $\nu \sim 110$–150 MHz. The increase in radiative efficiency

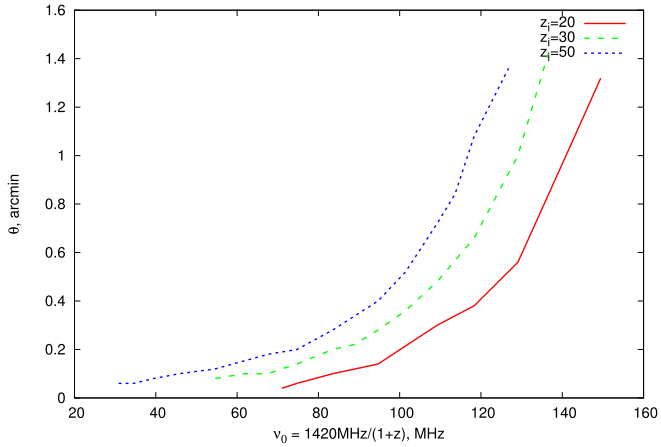

Figure 4. Dependence "angular diameter–observed frequency" for spheres emitted in the H I 21 cm line around a growing BH with a radiative efficiency $\epsilon = 0.1$ starting its evolution at redshifts $z_0 = 50$, 30, and 20 (lines from left to right). The diameter of the spheres is determined as the location where the brightness temperature in the 21 cm H I line $\Delta T_b^{\rm H\,I}$ reaches maximum (see Figure 2).

obviously leads to larger angular size, e.g., it grows up to 1.7 arcmin at 150 MHz ($z = 8.5$).

Current radio interferometers such as LOFAR and the upcoming SKA1-LOW have the capability of detecting the contrast between the H I brightness temperature on angular scales of a few arcminutes. This contrast could be detected statistically, e.g., by measuring the two-point correlation function of the intensity of the redshifted H I line, or by imaging.[6] Our analysis can be extended to predict the two-point functions of the spatial distribution of H I, but we do not attempt it here partly because these functions depend on the fraction of the universe in which the thermal and ionization history is affected by early BHs (e.g., Zaldarriaga et al. 2004); this fraction cannot be reliably computed because the space density of the precursor of these BHs is highly uncertain, as already noted above. For imaging, the projected sensitivity of the SKA is expected to reach a few millikelvin on angular scales from 1 to 10 arcmin (Koopmans et al. 2015). The expected contrast (Figure 2), particularly in light of the recent EDGES result, is likely to reach a few hundred millikelvin, which is easily detectable by SKA1-LOW and possibly by LOFAR.

4.1.1. Altered Thermodynamics from DM Cooling

We discuss next the impact of an altered thermal history on cosmological observables caused by additional cooling of baryons in elastic interactions with dark matter (Bowman et al. 2018). We show the impact of the global thermal state of the neutral gas implied by this result in Figure 5. Closer to the BH, the thermal and ionization state of the gas is determined by the emission from the BH. However, unlike the case shown in Figure 2, the H I signal is seen in strong absorption far away from the BH in the redshift range 15–19, in agreement with EDGES results discussed above.

For comparison, in Figure 6 we show a similar model without baryon cooling forced by elastic interactions with dark matter, but with heating from energy released in initial episodes

[6] For a discussion of the sensitivities for these two observables in radio interferometry, see, e.g., Sethi & Haiman (2008).

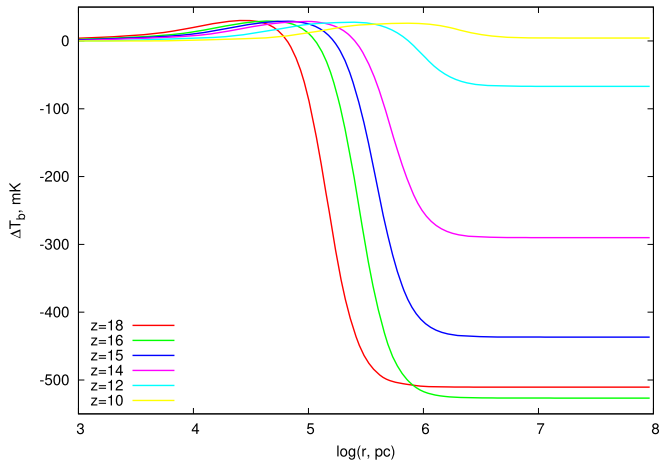

Figure 5. Brightness temperature in the 21 cm H I line vs. radius around a BH with initial mass $M_{\mathrm{BH},z0} = 300\,M_\odot$, $\epsilon = 0.1$ and $z_0 = 40$, with altered thermodynamics of baryons due to elastic scattering with cold dark matter.

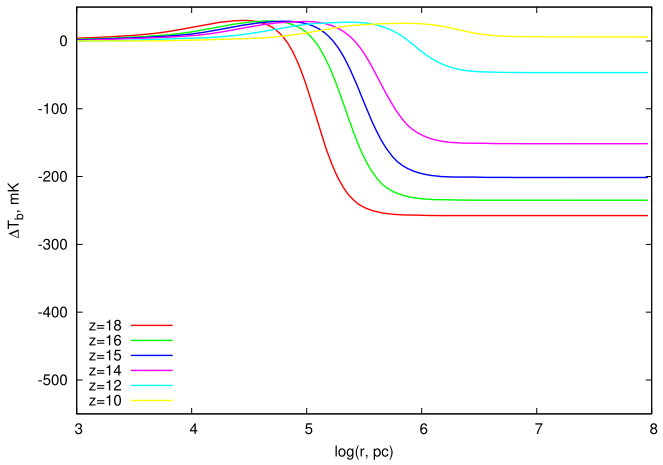

Figure 6. Same as in Figure 5 without baryon cooling due to elastic collisions with dark matter, but with an additional heating coming from energy released by stars in the first episode of star formation.

of star formation, as in Fialkov et al. (2014) and Cohen et al. (2017). An obvious distinctive feature of models with DM cooling is that outside the zone of influence, the brightness temperature follows the global behavior of the H I spin temperature. This situation causes strong spatial contrast in the H I brightness temperature in the redshift range of interest, which makes it easier to observe this signal with current and future radio interferometers.

4.2. Dependences on Initial Parameters

Minihalos are thought to form in high peaks of the cosmological density field. Even though for higher redshifts such peaks become rarer, minihalos can form as early as $z \sim 50$ (Gao et al. 2005). Such minihalos can host first BHs, which in turn can become progenitors of SMBHs $M \sim 10^9\,M_\odot$ found at $z \sim 6$–7 (e.g., Mortlock et al. 2011; Wu et al. 2015). We briefly discuss possible observational manifestations of BHs that began growing at higher redshifts.

One obvious consequence of a BH growing at higher redshift is the larger radius of the zone of influence at a given z. For instance, the size of the zone around a BH growing from $z_0 = 25$ is greater than that of a BH at $z_0 = 20$ by about 60% at $z = 16.5$ (the corresponding 21 cm line shifts to 80 MHz) and 30% at $z = 9$ (the corresponding line peak frequency is 142 MHz). The brightness temperature magnitude decreases from 5.7 mK at 80 MHz to 1.8 mK at 142 MHz, with a weak dependence on the initial redshift z_0.

Another important issue concerns the mass budget of a growing BH. Dark matter halos that host BHs should have a sufficient amount of baryons to feed the BH. This requirement is especially critical for lower values of the radiative efficiency ϵ. As mentioned above, for $\epsilon = 0.1$, a BH mass grows by roughly a factor 2.5×10^3 in ∼400 Myr evolution, but the factor reaches 1.5×10^7 for $\epsilon = 0.05$. In such halos the H I column density might be higher than the fiducial value adopted here, $N_{\mathrm{H\,I}} = 10^{20}\,\mathrm{cm}^{-2}$. An increase of the H I column density causes the brightness temperature radial profiles to shrink. For example, for $N_{\mathrm{H\,I}} = 10^{21}\,\mathrm{cm}^{-2}$, the peak of the 21 cm brightness temperature for $z = 16.5$ shifts from $r \sim 7$ kpc, corresponding to the fiducial H I column density, to ∼3 kpc. However, later on, this difference diminishes, e.g., the ratio between the radii becomes about 1.3 at $z = 8.5$. The difference in sizes of the zone where $\Delta T_b > 0$ is smaller and becomes negligible for the final redshift.

The masses of stellar BHs formed by very massive stars remains uncertain. It is conceivable that the initial mass of a BH may be either lower or higher than the fiducial value $M_{\mathrm{BH},t=0} = 300\,M_\odot$. As expected, more massive BHs produce larger zones of influence. The radius of the zone at which the brightness temperature in the H I 21 cm line reaches maximum depends on the initial mass of a BH seed as $r \sim M_{\mathrm{BH},t=0}^{0.38} \exp(z^{-1.16})$ for $\epsilon = 0.1$ and $M_{\mathrm{BH},t=0} = (30 - 10^3)\,M_\odot$. For example, its radius increases by about a factor 1.5 for $M_{\mathrm{BH},t=0} = 10^3\,M_\odot$ until $z = 8.5$ if a BH starts growing $z_0 = 20$.

The size of the zone of influence around a growing BH depends on the slope α of the spectral energy distribution (2), which might vary from -1.7 to -1.4. A flatter spectrum leads to a larger radius of the zone, whereas a steeper one produces a smaller zone. For instance, the zone around a growing BH with $\alpha = -1.7$ is ∼20%–25% smaller than that for the fiducial value $\alpha = -1.5$.

Finally, we consider how heating and the Lyα background affect the evolution of the zones of influence around growing BHs. Resonance and high-energy photons produced due to the initial episode of star formation provide a homogeneous background in this case. Figures 2 and 6 show the H I signal around a halo with a growing BH immersed in the IGM that evolved adiabatically and was exposed to both X-ray and Lyα background photons, as in Fialkov et al. (2014) and Cohen et al. (2017). These models represent extreme cases: in the former there is no external background radiation, whereas the latter includes a strong (maximum in the sense that $T \simeq T_s$) Lyα pumping rate and heating from background ionizing photons. We combine the expected H I signals for these models in Figure 7. The growth of the brightness temperature in the model with heating is due to the strong Lyα background. The size of the influence zone increases with decreasing redshift in presence of the background. At $z = 10$, the size doubles as compared to that in the model without the background radiation. At high redshifts, where heating is weak, this increase is small.

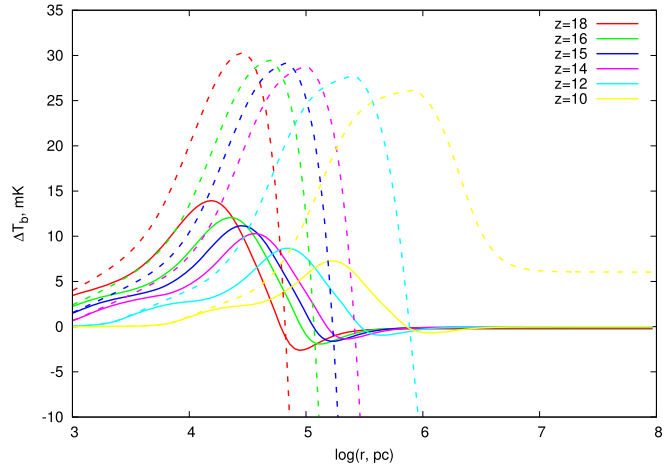

Figure 7. Brightness temperature in the 21 cm H I line vs. radius around a BH with initial mass $M_{\rm BH,z_0} = 300\,M_\odot$, $\epsilon = 0.1$ and $z_0 = 40$, without (solid lines) and with (dashed lines) an additional heating coming from energy released by stars in the first episode of star formation.

4.3. ^{3}He II Hyperfine Line

As discussed above, the other potential observable is the ^{3}He II hyperfine line. Unlike massive stars, which can also ionize He II (e.g., Tumlinson & Shull 2000), BHs can form large He II and even He III ionization zones. Figure 1 presents the radial distribution of the He II fraction around BHs with a constant and a growing mass. The size of the He II region around BH with constant mass of several hundred solar masses is about 1–3 kpc, that is, compared to the virial radius of the host dark matter minihalo. However, it increases by several ten or even hundred times around a growing BH. Such zones can emit in the hyperfine structure line of a singly ionized helium-3 isotope. The brightness temperature in the ^{3}He II line reaches several ten nanoK (Figure 8), and the size of the emission zone can extend up to more than 10 kpc.

The angular size of such zones at frequency $\sim$1 GHz is 0.3–0.4 arcmin, as shown in Figure 9. The upcoming radio interferometer SKA1-MID can reach a flux sensitivity of sub-micro-Jansky at such frequencies at these angular scales (Ahn et al. 2015), which corresponds to a brightness temperature sensitivity that is still orders of magnitude higher than the expected signal. Therefore it is unlikely that this signal would be detected by upcoming radio interferometers.

4.4. nα H I Recombination Lines

We next consider recombination lines arising from ionized regions surrounding the accreting BH.

Figure 10 presents the flux in the Hα line (left panel) from partially ionized spheres around a BH starting its evolution at $z_0 = 20$. The size of regions that dominate emission in Hα line is $\simeq$10 kpc. The flux for $\epsilon \sim 0.05$ exceeds μJy at $z \lesssim 11$. The angular size of such a region is $\simeq 0\farcs2$, which can be resolved by the *JWST*, which has angular resolution of $\simeq 0\farcs05$ (e.g., Kalirai 2018). The redshifted Hα line has a wavelength $\simeq$7.8 μm for this case, which is accessible to the mid-infrared (MIRI) instrument on board the *JWST*. Around this wavelength, a source of flux $\simeq$0.2 μJy can be detected with a signal-to-noise ratio S/N = 10 in an integration time of 10^4 s. As this sensitivity corresponds to sources within the resolution element of the instrument ($\simeq 0\farcs05$) and the source angular size is nearly four times the resolution, the detection sensitivity decreases by nearly a factor of 4. A comparison of this estimate of sensitivity with the fluxes shown in Figure 10 shows that the regions of influence around BHs with $\epsilon \sim 0.05$ (starting its growth at $z_0 = 20$) can be detected for $z \simeq 10$–12. For BHs with a higher radiation efficiency $\epsilon \sim 0.1$, the surrounding gas might be observable at $z \sim 8.5$ in Hα.

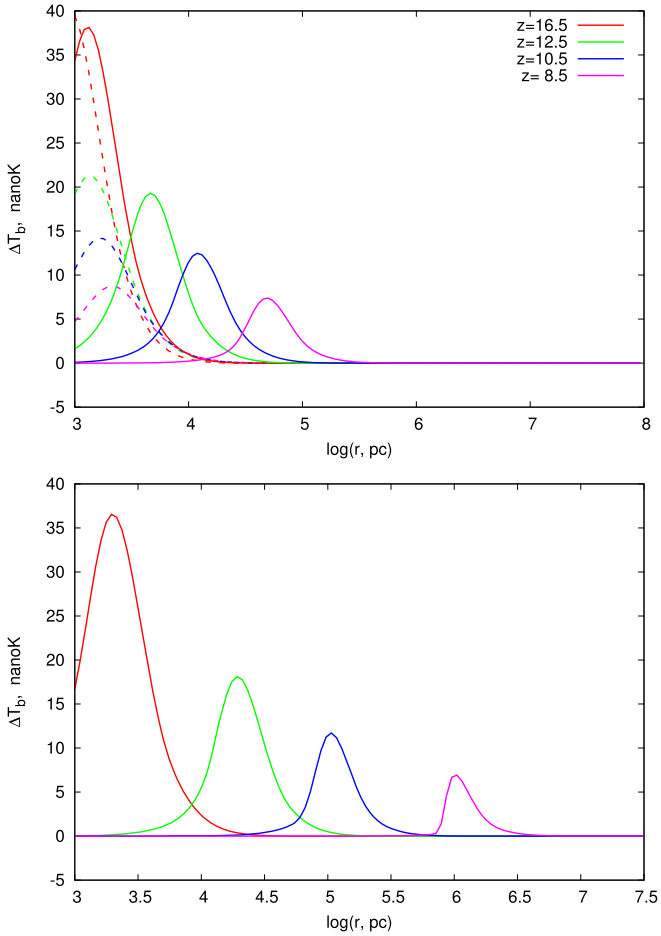

Figure 8. Same as in Figure 2 for the ^{3}He II 3.46 cm line.

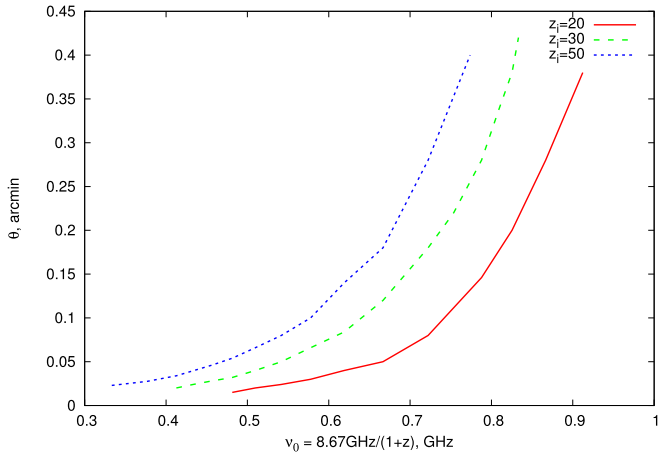

Figure 9. Dependence "angular diameter–observed frequency" for spheres emitted in the ^{3}He II 3 cm line around a growing BH with a radiative efficiency $\epsilon = 0.1$, starting its evolution at redshifts $z_0 = 50$, 30, and 20 (lines from left to right). The diameter of spheres is defined as the location where the brightness temperature in the line $\Delta T_b^{\rm ^3He\ II}$ reaches maximum (see Figure 8).

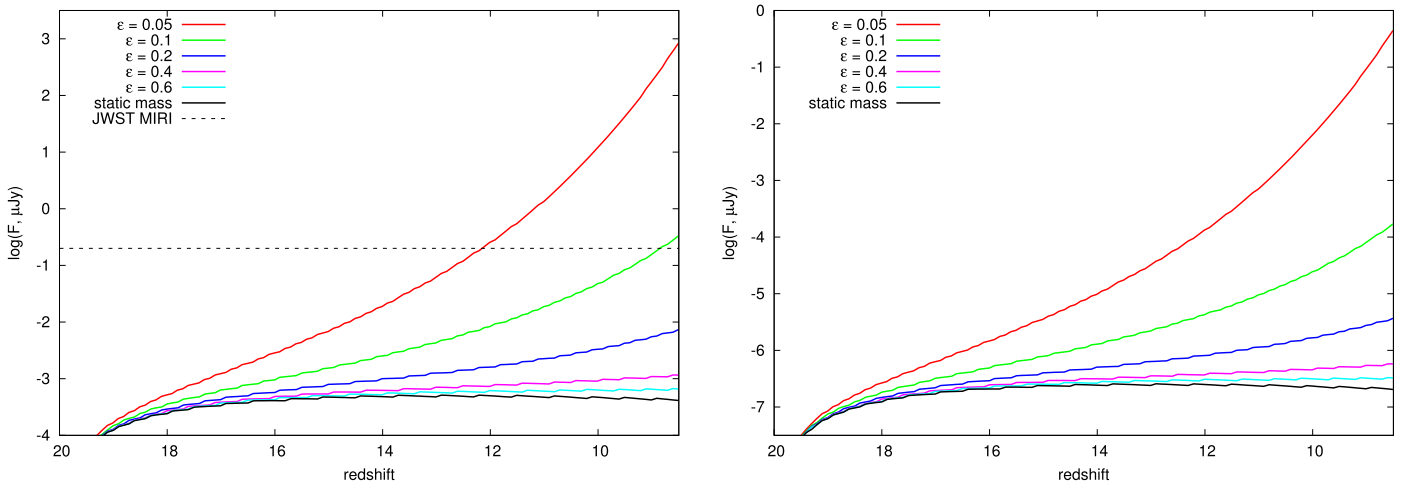

Figure 10. Fluxes in the Hα (left panel) and Hnα, $n = 30$, (right panel) recombination lines that can be detected from partially ionized spheres around a BH with an initial mass $M_{\rm BH,z_0} = 300\,M_\odot$ starting its evolution at $z_0 = 20$ for several radiative efficiencies $\epsilon = 0.05$, 0.1, 0.2, 0.4, and 0.6 and a static BH mass $M_{\rm BH} = 300\,M_\odot$ (lines from top to bottom).

Expected fluxes from transitions for $n = 30$ (Figure 10, right panel) are near the thresholds of modern radio telescopes only around very rapidly growing BHs ($\epsilon = 0.05$). It should be noted that it is much easier to detect an n, $n-1$ transition for smaller n as the flux of the line $\varepsilon \sim n^{-2.72}$.

5. Conclusions

In this paper, we considered the impact of a growing BH on the thermal and ionization state of the IGM in the redshift range $8 < z < 25$, and discussed possible observables that can probe this influence. We have found that the sizes of zones of ionized gas around growing BHs are greater than that for a non-growing BH: for accretion with a radiative efficiency $\epsilon = 0.1$, they are more than one order of magnitude larger at redshift $z = 8.5$. The physical size of a zone of influence increases from nearly 10 to 300 kpc during the growth of a BH. The greatest part of this region contains highly ionized hydrogen up to a reasonable fraction of unity, and the temperature exceeds 300 K. The helium ionization region is generally smaller and reaches a maximum of 100 kpc.

We consider three observables as a probe of growing primordial BHs.

We show that the influence region of the 21 cm emission around an accreting BH with a radiative efficiency $\epsilon \gtrsim 0.05$–0.1 could be in the range of a few hundred kiloparsec to 1 Mpc (Figure 2). The angular scale of this emission and the spatial contrast of the H I signal is accessible to current and upcoming radio telescopes such as SKA1-LOW. We also consider the impact of recent EDGES observations (Bowman et al. 2018) and show that it greatly enhances the expected contrast (Figure 5).

We also study the emission of the hyperfine line of ^{3}He II ($\lambda = 3.4$ cm) from regions surrounding the growing BH. The brightness temperatures in these lines could reach tens of nano-Kelvin. Taking into account the sizes of these regions, we anticipate that this emission cannot be detected by the upcoming radio telescope SKA1-MED.

We finally consider the hydrogen recombination lines (n, n–1) from ionized regions surrounding growing BHs. The Hα line provides the best prospect of detection (Figure 10); the *JWST* can detect this line with an S/N = 10 in ten thousand seconds of integration. The expected fluxes from transitions between higher levels (e.g., Figure 10 for $n = 30$) are near the thresholds of modern radio telescopes only around very rapidly growing BHs.

In sumary, we model emission from an accreting primordial BH and study its impact on the ionization and thermal state of the surrounding medium. We also consider the prospects of the detection of this dynamical process in the redshift range $8.5 < z < 25$.

In conclusion, we note that the observability of the features we discuss in the paper would be greatly boosted if the precursors of SMBHs could be detected at high redshifts. This possibility has been studied by Valiante et al. (2018a, 2018b). Their analysis suggests that future missions such as the *JWST* will be able to detect high-mass BH seeds at $z \sim 16$ directly.

We are grateful to the referee for a careful reading of the manuscript and very detailed comments. This work is supported by the joint RFBR-DST project (RFBR 17-52-45063, DST P-276). The work by Y.S. is done under partial support from the joint RFBR-DST project (17-52-45053), and the Program of the Presidium of RAS (project code 28). The code for the thermal evolution has been developed under support by Russian Scientific Foundation (14-50-00043). E.V. is thankful to the Ministry for Education and Science of the Russian Federation (grant 3.858.2017/4.6).

References

Abel, T., Bryan, G. L., & Norman, M. L. 2002, Sci, 295, 93
Ahn, K., Mesinger, A., Alvarez, M. A., & Chen, X. 2015, in Proc. Advancing Astrophysics with the Square Kilometre Array (AASKA14) (Trieste: PoS), 3, http://pos.sissa.it/cgi-bin/reader/conf.cgi?confid=215,id.3
Ali, Z. S., Parsons, A. R., Zheng, H., et al. 2015, ApJ, 809, 61
Bagla, J. S., & Loeb, A. 2009, MNRAS, arXiv:0905.1698
Bañados, B., Venemans, B. P., Mazzucchelli, C., et al. 2017, Natur, 553, 473
Barkana, R. 2018, Natur, 555, 71
Barkana, R., & Loeb, A. 2001, PhR, 349, 125
Barkana, R., Outmezguine, N. J., Redigolo, D., & Volansky, T. 2018, arXiv:1803.03091
Beardsley, A. P., Hazelton, B. J., Sullivan, I. S., et al. 2016, ApJ, 833, 102
Becerra, F., Greif, T. H., Springel, V., & Hernquist, L. E. 2015, MNRAS, 446, 2380

Begelman, M. C., Volenteri, M., Rees, M. J., et al. 2006, MNRAS, 370, 289
Bell, M. B. 2000, ApJ, 531, 820
Berlin, A., Hooper, D., Krnjaic, G., & McDermott, S. D. 2018, PhRvL, 121, 011102
Bowman, J. D., Rogers, A. E. E., Monsalve, R. A., Mozdzen, T. J., & Mahesh, N. 2018, Natur, 555, 67
Bromm, V., Coppi, P. S., & Larson, R. B. 2002, ApJ, 564, 23
Bromm, V., Ferrara, A., Coppi, P. S., & Larson, R. B. 2001, MNRAS, 328, 969
Bromm, V., & Larson, R. B. 2004, ARA&A, 42, 79
Bromm, V., Yoshida, N., & Hernquist, L. 2003, ApJL, 596, L135
Cen, R. 1992, ApJ, 78, 341
Chen, X., & Miralda-Escudé, J. 2004, ApJ, 602, 1
Chen, X., & Miralda-Escudé, J. 2008, ApJ, 684, 18
Chuzhoy, L., & Kolb, E. W. 2009, JCAP, 7, 14
Ciardi, B., & Ferrara, A. 2004, SSRv, 116, 625
Cohen, A., Fialkov, A., Barkana, R., & Lotern, M. 2017, MNRAS, 472, 1915
Dijkstra, M., Ferrara, A., & Mesinger, A. 2014, MNRAS, 442, 2036
Dopcke, G., Glover, S. C. O., Clark, P. C., & Klessen, R. S. 2013, ApJ, 766, 103
Draine, B. T. 2011, Physics of the Interstellar and Intergalactic Medium (Princeton, NJ: Princeton Univ. Press)
Draine, B. T., & Miralda-Escudé, J. 2018, ApJL, 858, L10
Dvorkin, C., Blum, K., & Kamionkowski, M. 2014, PhRvD, 89, 023519
Fan, X., Carilli, C. L., & Keating, B. 2006, ARA&A, 44, 415
Feng, C., & Holder, G. 2018, ApJL, 858, L17
Ferrara, A., & Loeb, A. 2013, MNRAS, 431, 2826
Fialkov, A., Barkana, R., & Cohen, A. 2018, PhRvL, 121, 011101
Fialkov, A., Barkana, R., & Visbal, E. 2014, Natur, 506, 197
Field, G. B. 1958, PIRE, 46, 240
Furlanetto, S. R., Oh, S. P., & Briggs, F. H. 2006, PhR, 433, 181
Gao, L., White, S. D. M., Jenkins, A., Frenk, C. S., & Springel, V. 2005, MNRAS, 363, 379
Gaspari, M., & Sądowski, A. 2017, ApJ, 837, 149
Glover, S. C. O., & Jappsen, A.-K. 2007, ApJ, 666, 1
Gnedin, N. Y., & Shaver, P. A. 2004, ApJ, 608, 611
Goldwire, H. C., Jr, & Goss, W. M. 1967, ApJ, 149, 15
Greif, T. H., Johnson, J. L., Bromm, V., & Klessen, R. S. 2007, ApJ, 670, 1
Haiman, Z., Abel, T., & Rees, M. J. 2000, ApJ, 534, 11
Haiman, Z., Thoul, A. A., & Loeb, A. 1996, ApJ, 464, 523
Hills, R., Kulkarni, G., Meerburg, P. D., & Puchwein, E. 2018, arXiv:1805.01421
Hosokawa, T., Omukai, K., Yoshida, N., & Yorke, H. W. 2011, Sci, 334, 1250
Jeon, M., Pawlik, A. H., Greif, T. H., et al. 2012, ApJ, 754, 34
Johnson, J. L., Khochfar, S., Greif, T. H., & Durier, F. 2011, MNRAS, 410, 919
Kalirai, J. 2018, ConPh, 59, 251
Khandai, N., Di Matteo, T., Croft, R., et al. 2015, MNRAS, 450, 1349
Koopmans, L., Pritchard, J., Mellema, G., et al. 2015, in Advancing Astrophysics with the Square Kilometre Array (AASKA14) (Trieste: PoS), 1
Kuhlen, M., Madau, P., & Montgomeri, R. 2006, ApJL, 637, 1
Kulkarni, G., Choudhury, T. R., Puchwein, E., & Haehnelt, M. G. 2016, MNRAS, 463, 2583
Latif, M. A., & Ferrara, A. 2016, PASA, 33, 51
Latif, M. A., Volonteri, M., & Wise, J. H. 2018, MNRAS, 476, 5016
Liszt, H. 2001, A&A, 371, 698
Lusso, E., Worseck, G., Hennawi, J. F., et al. 2015, MNRAS, 449, 4204
Madau, P., Meiksin, A., & Rees, M. J. 1997, ApJ, 475, 429
Matsuoka, Y., Onoue, M., Kashikawa, N., et al. 2016, ApJ, 828, 26
McDermott, S. D., Yu, H.-B., & Zurek, K. M. 2011, PhRvD, 83, 063509
McLure, R. J., & Dunlop, J. S. 2004, MNRAS, 352, 1390
McQuinn, M., & Switzer, E. R. 2009, PhRvD, 80, 063010
McQuinn, M., Zahn, O., Zaldarriaga, M., Hernquist, L., & Furlanetto, S. R. 2006, ApJ, 653, 815
Mesinger, A., Ewall-Wice, A., & Hewitt, J. 2014, MNRAS, 439, 3262
Morales, M. F. 2005, ApJ, 619, 678
Morales, M. F., & Wyithe, J. S. B. 2010, ARA&A, 48, 127
Mortlock, D. J., Warren, S. J., Venemans, B. P., et al. 2011, Natur, 474, 616
Muñoz, J. B., & Loeb, A. 2018, Natur, 557, 684
Naoz, S., Noter, S., & Barkana, R. 2006, MNRAS, 373, 98
Negri, A., & Volonteri, M. 2017, MNRAS, 467, 3475
Paciga, G., Albert, J. G., Bandura, K., et al. 2013, MNRAS, 433, 639
Palanque-Delabrouille, N., Magneville, Ch., Yèche, Ch., et al. 2013, A&A, 551A, 29
Park Ricotti, M. 2011, ApJ, 739, 2
Parsons, A., Pober, J., McQuinn, M., Jacobs, D., & Aguirre, J. 2012, ApJ, 753, 81
Patil, A. H., Yatawatta, S., Koopmans, L. V. E., et al. 2017, ApJ, 838, 65
Pen, U.-L., Chang, T.-C., Hirata, C. M., et al. 2009, MNRAS, 399, 181
Planck Collaboration, Ade, P. A. R., Aghanim, N., et al. 2016, A&A, 594, A13
Pritchard, J. R., & Loeb, A. 2008, PhRvD, 78, 103511
Ricotti, M., Gnedin, N. Y., & Shull, J. M. 2002, ApJ, 575, 33
Rood, R. T., Wilson, T. L., & Steigman, G. 1979, ApJL, 227, L97
Rosas-Guevara, Y., Bower, R. G., Schaye, J., et al. 2016, MNRAS, 462, 190
Rule, E., Loeb, A., & Strelnitskii, V. S. 2013, ApJL, 775, 17
Rybicki, G. B., & Lightman, A. P. 2004, Radiative Processes in Astrophysics (New York: Wiley-VCH)
Scott, J. E., Kriss, G. A., Brotherton, M., et al. 2004, ApJ, 615, 135
Seager, S., Sasselov, D., & Scott, D. 2000, ApJS, 128, 407
Sethi, S., & Haiman, Z. 2008, ApJ, 673, 1
Sethi, S. K. 2005, MNRAS, 363, 818
Shapiro, S. L. 2005, ApJ, 620, 59
Shull, J. M., Stevans, M., & Danforth, C. W. 2012, ApJ, 752, 162
Shull, J. M., & van Steenberg, M. E. 1985, ApJ, 298, 268
Sijacki, D., Vogelsberger, M., Genel, S., et al. 2015, MNRAS, 452, 575
Stevans, M. L., Shull, J. M., Danforth, C. W., & Tilton, E. M. 2014, ApJ, 794, 75
Sunyaev, R. A. 1966, AZh, 43, 1237
Takeuchi, Y., Zaroubi, S., & Sugiyama, N. 2014, MNRAS, 444, 2236
Tan, J. C., & McKee, C. F. 2004, ApJ, 603, 383
Tegmark, M., Silk, J., Rees, M. J., et al. 1997, ApJ, 474, 1
Telfer, R. C., Zheng, W., Kriss, G. A., & Davidsen, A. F. 2002, ApJ, 565, 773
Townes, C. H. 1957, in Proc. IAU Symp. 4, Radio Astronomy, ed. H. C. van de Hulst (Cambridge: Cambridge Univ. Press), 92
Tozzi, P., Madau, P., Meiksin, A., & Rees, M. J. 2000, ApJ, 528, 597
Tumlinson, J., & Shull, J. M. 2000, ApJL, 528, 65
Valiante, R., Schneider, R., Zappacosta, L., et al. 2018a, MNRAS, 474, 3825
Valiante, R., Schneider, R., Zappacosta, L., et al. 2018b, MNRAS, 476, 407
Vasiliev, E. O., Vorobyov, E. I., Matvienko, E. E., Razoumov, A. O., & Shchekinov, Yu. A. 2012, ARep, 56, 895
Vasiliev, E. O., Vorobyov, E. I., & Shchekinov, Yu. A. 2008, A&A, 489, 505
Venemans, B. P., Bañados, E., Decarli, R., et al. 2015, ApJL, 801, 11
Venemans, B. P., Findlay, J. R., Sutherland, W. J., et al. 2013, ApJ, 779, 24
Volonteri, M., Dubois, Y., Pichon, C., & Devriendt, J. 2016, MNRAS, 460, 2979
Volonteri, M., & Rees, M. J. 2005, ApJ, 633, 624
Volonteri, M., & Rees, M. J. 2006, ApJ, 650, 669
Weinberger, R., Springel, V., Pakmor, R., et al. 2018, MNRAS, 479, 4056
Whalen, D., Abel, T., & Norman, M. L. 2004, ApJ, 610, 14
Whalen, D., van Veelen, B., O'Shea, B. W., & Norman, M. L. 2008, ApJ, 682, 49
Whalen, D. J., & Fryer, C. L. 2012, ApJL, 756, L19
Wise, J. H. 2018, in Growth and Feedback from the First Black Holes, ed. M. Latif & D. R. G. Schleicher (Singapore: World Scientific), in press (arXiv:1807.06080)
Woosley, S. E., Heger, A., & Weaver, T. A. 2002, RvMP, 74, 1015
Wouthuysen, S. 1952, AJ, 57, 31
Wu, X.-B., Wang, F., Fan, X., et al. 2015, Natur, 518, 512
Yoshida, N., Omukai, K., & Hernquist, L. 2008, Sci, 321, 669
Zaldarriaga, M., Furlanetto, S. R., & Hernquist, L. 2004, ApJ, 608, 622
Zaroubi, S. 2013, in The First Galaxies, Astrophysics and Space Science Library, Vol. 396 (Berlin: Springer), 45